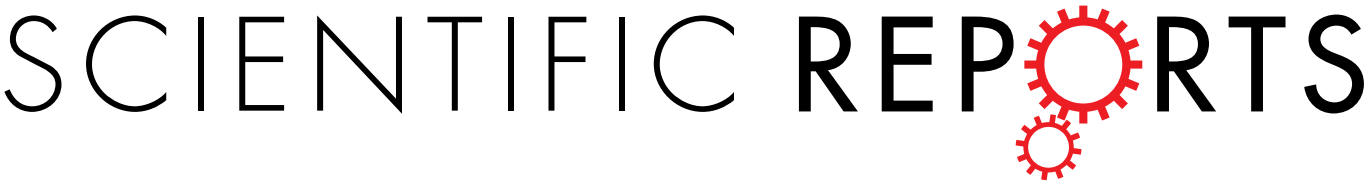

OPEN

Eu^{3+}-doped $Bi_4Si_3O_{12}$ red phosphor for solid state lighting: microwave synthesis, characterization, photoluminescence properties and thermal quenching mechanisms

Received: 02 June 2016
Accepted: 11 January 2017
Published: 15 February 2017

Yan Zhang, Jiayue Xu, Qingzhi Cui & Bobo Yang

Europium-doped bismuth silicate ($Bi_4Si_3O_{12}$) phosphor has been prepared by microwave irradiation method and its crystal structure is determined using Rietveld method. As-prepared phosphor consists of spherical, monodispersed particles with few agglomeration, high crystallinity, and narrow grain size distribution. The phosphor can be efficiently excited in the wavelength range of 260–400 nm, which matched well with the emission wavelengths of NUV LED chips. The photoluminescence spectra exhibit the highest emission peak at 703 nm originating from $^5D_0 \rightarrow {}^7F_4$ transition of Eu^{3+} under NUV excitation. The luminescence lifetime for $Bi_4Si_3O_{12}$: 2 at% Eu^{3+} phosphor decreases from 2.11 to 1.86 ms with increasing temperature from 10 to 498 K. This behavior of decays is discussed in terms of radiative and nonradiative decays dependence on temperature. The thermal quenching mechanism of $^5D_0$ emission of Eu^{3+} in $Bi_4Si_3O_{12}$ phosphor is a crossover process from the $^5D_0$ level of Eu^{3+} to a ligand-to-europium ($O^{2-} \rightarrow Eu^{3+}$) charge transfer state. The quantum efficiency of the phosphor under 393 nm excitation is found to be 14.5%, which is higher than that of the commercial red phosphors Y_2O_3: Eu^{3+}, Y_2O_2S: Eu^{3+}. The temperature effect on CIE coordinate was discussed in order to further investigate the potential applications.

White light-emitting-diodes (WLEDs) as the next-generation general lighting source is extensively studied due to high efficiency, long lifetime, fast response, energy saving and environment friendliness etc[1,2]. Presently, the commercial WLEDs comprises a blue LED chip with yellow phosphor YAG: Ce^{3+} [3]. However, YAG-based white LEDs suffers from poor color rending index (CRT) ($Ra < 80$) and high correlated color temperature ($CCT > 5000$ K) due to the lack of red light component. A combination of near-ultraviolet (NUV) LED chip with tricolor (red, green and blue) (RGB) phosphors or a combination of R/G phosphors with a blue LED chip is another strategy to generate white LEDs. The WLEDs fabricated by this strategy can provide high color rending index ($Ra > 90$)[4], appropriate color temperature and high color tolerance to chip's variation[5,6]. The WLEDs based on NUV LED chip coated with tricolor phosphor is not widely used owing to the lack of red phosphors with high conversion efficiency. The commonly used sulphide based red phosphor (Y_2O_2S: Eu^{3+}) in WLEDs could not efficiently absorb NUV light emitted by NUV LED chip[7]. Therefore, the demand for new red phosphors, which can emit suitable red light for inclusion with the blue LED-YAG: Ce^{3+} combination, is very urgent.

In the search of red emitting phosphors that can be pumped by near-UV or blue emitting LEDs, the nitride based red phosphors and Mn^{4+} -doped activated oxide/fluoride red phosphors emerged as attractive red phosphor for white LED[8–13]. The nitrides (e.g., $Ca_2Si_5N_8$: Eu^{2+} [14], $CaAlSiN_3$: Eu^{2+} [15], (Sr, Ca)$AlSiN_3$: Eu^{2+} [16]) and oxynitrides ($SrSi_2O_2N_2$: Eu^{2+} [17]) seem to be promising candidates; unfortunately, the high cost caused by the rather demanding synthesis and lower luminous efficacy resulting from broad emission band limit their practical application. Mn^{4+} doped oxide phosphors with broad band emissions exhibit weak absorption for blue excitation light, and Mn^{4+} doped fluoride phosphors are suffering from thermal stability and high humidity degradation[18].

School of Materials science and Engineering, Shanghai Institute of Technology, Shanghai 201418, P.R. China. Correspondence and requests for materials should be addressed to Y.Z. (email: zhang.yan@vip.163.com) or J.X. (email: xujiayue@sit.edu.cn)

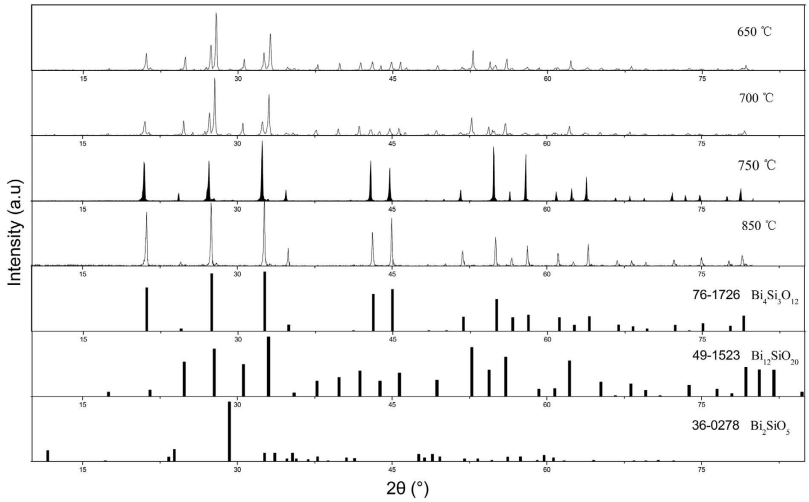

Figure 1. Powder X-ray diffractograms of microwave-prepared $Bi_4Si_3O_{12}$: 2 at% Eu^{3+}.

The optimal red-emitting phosphor for a warm-white LED with a high quantum efficiency and high color quality has a narrow emission band (FWHM < 30 nm) located between 615 and 655 nm[19]. Eu^{3+} doped phosphors are probably the better choice because Eu^{3+}-doped phosphors exhibit higher luminescence efficiency and stronger red emission compared with other luminous materials, due to the facts that Eu^{3+} ($4f^6$) ion emits a narrow band, almost monochromatic light and has a long lifetime of the optically active states[20–27].

With good physical, chemical and mechanical properties, bismuth silicate ($Bi_4Si_3O_{12}$) is a well-known scintillator and also used as the host for lasers and phosphors[28–31]. The conventional preparative methods for this phosphor require temperature in the range of 850–1000 °C and several hours soaking time[32,33]. $Bi_4Si_3O_{12}$ obtained from this method encounters a few problems, such as inhomogeneity, low surface area and broad particle size distribution. In microwave system, since microwave irradiation directly couple microwave energy to the molecules that are present in the reaction mixture, rather than being supplied from the external, uniform and rapid heating can be realized within a short time and at a temperature lower than that normally required. Therefore, compared with the conventional methods, microwave irradiation offers several advantages, including reduced reaction time, small particle size, narrow particle size distribution, better selectivity, and higher reaction yield[34,35]. This route leads a mixture at the molecular level of the constituent and better product purity. Different types of nanoparticles such as metal, semiconductors, and oxides have been synthesized using microwave irradiation[36–41].

In this work we report the preparation of the Eu-doped $Bi_4Si_3O_{12}$ phosphors processed by microwave synthesis route. The structure, morphology and particle size distribution of the $Bi_4Si_3O_{12}$: Eu phosphors have been studied by means of X-ray diffraction (XRD), scanning electronic microscopy (SEM), and laser particle size analyzer. The temperature dependence of the luminescence properties and the decay time are investigated and discussed for the phosphors. And the thermal quenching mechanisms as well as the quantum efficiency and temperature dependence of the CIE chromaticity of Eu^{3+} in the $Bi_4Si_3O_{12}$ matrix are also discussed.

Results and Discussion

Structural and morphology characterization. The XRD patterns of the as-obtained $Bi_4Si_3O_{12}$: 2 at% Eu^{3+} powder obtained at various microwave irradiation temperature are exhibited in Fig. 1. For the samples prepared by the microwave synthesis method, the $Bi_{12}SiO_{20}$ and Bi_2SiO_5 phases are observed as impurity phases when the calcination temperatures are 650, 700, 800 °C. When the irradiation temperature is 750 °C, a single phase of $Bi_4Si_3O_{12}$: 2 at% Eu^{3+} is obtained. And the XRD pattern of the target material is shown in Fig. 1. It indicates that microwave heating provides satisfactory conditions for the formation of single phase $Bi_4Si_3O_{12}$: 2 at% Eu^{3+} in a short time of 900 s at a low calcined temperature of 750 °C.

The Rietveld refinement is accomplished to obtain the detailed crystal structure information on Eu^{3+}-doped $Bi_4Si_3O_{12}$ phosphor. The single crystal structure data of $Bi_4Si_3O_{12}$ (ICSD No. 84519) are used as the starting structure model for the refinement. Figure 2 shows the observed, calculated, and difference XRD patterns for the Rietveld refinement of $Bi_4Si_3O_{12}$: 2at% Eu^{3+} phosphor. The reliability factors finally converges to goodness of fit parameters $\chi^2 = 4.17\%$, $R_{wp} = 9.84\%$ and $R_p = 7.10\%$, respectively, which shows the validity of the refinement process. The refinement results indicate that $Bi_4Si_3O_{12}$: 2at% Eu^{3+} phosphor is related to eulytine structure, and it has I-43d space group with unit cell parameters $a = b = c = 10.2831$ Å, $V = 1087.3625$ Å^3, and $Z = 4$. The crystallographic data and atom coordinate are summarized in Table 1. Figure 3 depicts the unit cell structure of $Bi_4Si_3O_{12}$ viewing along the *a*-direction and the coordination environment of cation sites.

According to ICSD No. 84519, pure $Bi_4Si_3O_{12}$ has a cubic structure with the I-43d space group, and its lattice parameters are $a = b = c = 10.2889$ Å. With Eu^{3+} incorporation into the $Bi_4Si_3O_{12}$ lattice, the XRD peaks slightly shift towards high 2θ range, implying the contraction of the lattice constants. Taking valence states, crystallochemical behavior and ionic radii of Bi^{3+} (117 pm), Si^{4+} (40 pm) and Eu^{3+} (108.7 pm) in consideration, Eu^{3+} ions replaced Bi^{3+} ions site easily. Thus, the substitution of Bi^{3+} ions with Eu^{3+} causes a decrease in the unit cell parameters in view of the fact that the ionic radii of Eu^{3+} (108.7 pm) is slightly smaller than that of Bi^{3+} (117 pm).

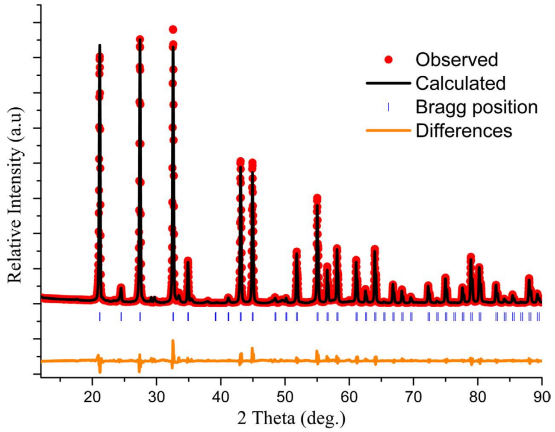

Figure 2. Rietveld refinement of the $Bi_4Si_3O_{12}$: 2 at% Eu^{3+} phosphor.

Formular	$(Bi_{0.98}Eu_{0.02})_4Si_3O_{12}$			
Crystal system	Cubic			
Space group	I -4 3 d			
Cell parameters	$a=b=c=10.2831$ Å			
	$\alpha=\beta=\gamma=90°$			
Cell Volume	1087.3625 Å^3			
Z	4			
R_{wp}	9.84%			
R_p	7.10%			
χ^2	4.17			
Atom	**Wyckoff position**	**Atoms coordinates**		
		x	***y***	***z***
Bi	16c	0.08503	0.08503	0.08503
Si	12a	0.37500	0.00000	0.25000
O	48e	0.06294	0.13624	0.29070

Table 1. Crystallographic data for $(Bi_{0.98}Eu_{0.02})_4Si_3O_{12}$ determined from Rietveld refinement.

Figure 4 shows the SEM images of $Bi_4Si_3O_{12}$: 2 at% Eu^{3+} phosphors prepared with microwave heating method and conventional solid state reaction method. In the case of the microwave heating method, the synthesized samples consisted of nearly spherical clusters of 0.6–0.8 μm in diameter. The results indicate that the microwave processing can effectively control the particle size and prevent heavy agglomeration, and thus is favorable to synthesis of fine particles of phosphors. On the other hand, when the conventional method was used, the particles aggregated to be consist of tightly packed smaller particles with size about 1–13 μm. This non-uniform particle size is caused due to the non-uniform distribution of temperature and mass flow during the synthesis. In addition, no sintering behavior found in the microwave heating may be attributed to rapid and uniform heating in a quite short time. Nanopowders with homogeneous grain size are an attractive feature for optical applications. In fact, it is well-known that the luminescence characteristics of the phosphor depend on the particle size[42].

The size distribution of the $Bi_4Si_3O_{12}$:2at% Eu^{3+} particle synthesized by microwave heating and solid state reaction methods is illustrated in Fig. 5. The single peak of particle size distribution is found for the phosphor. The sample exhibits a rather narrow size distribution concentrated in the regions of 694 nm–915 nm (average size 797 nm) with few aggregation or agglomeration. The conventional heating produces a broader particle size distribution of 1 to 10 μm (average size 7 μm). Compared with traditional high temperature solid state reaction, the microwave synthesis method offers advantage of being shorter reaction time for sample preparation. Therefore, the growth of grain size due to the rapid heating is prohibited in the reaction, and pure and single phase $Bi_4Si_3O_{12}$: Eu^{3+} particles with finer and uniform microstructure can be obtained by microwave irradiation method.

Excitation and emission spectra. The excitation spectrum of 2at% Eu^{3+}-doped $Bi_4Si_3O_{12}$ phosphor is recorded by monitoring the emission at 611 nm corresponding to the $^5D_0$–$^7F_2$ transition of Eu^{3+} (see Fig. 6). It consists of a broad absorption band along with a series of sharp peaks beyond 350 nm. The broad absorption band in 220–350 nm region (centered at 297 nm and 271 nm) is attributed to the transitions of $6s^2 \rightarrow 6s6p$ of Bi^{3+} ions, and Eu^{3+} charge transfer band (CTB), which is due to charge transfer from the filled $2p$ orbital of the O^{2-} to the partially filled $4f$ orbital of Eu^{3+}. It is well known that the ground state of Bi^{3+} ion with $6s^2$ configuration is $^1S_0$ level. The $6s6p$ configuration of Bi^{3+} ion yields the $^3P_0$, $^3P_1$, $^3P_2$ and $^1P_1$ excited states. In view of the spin selection

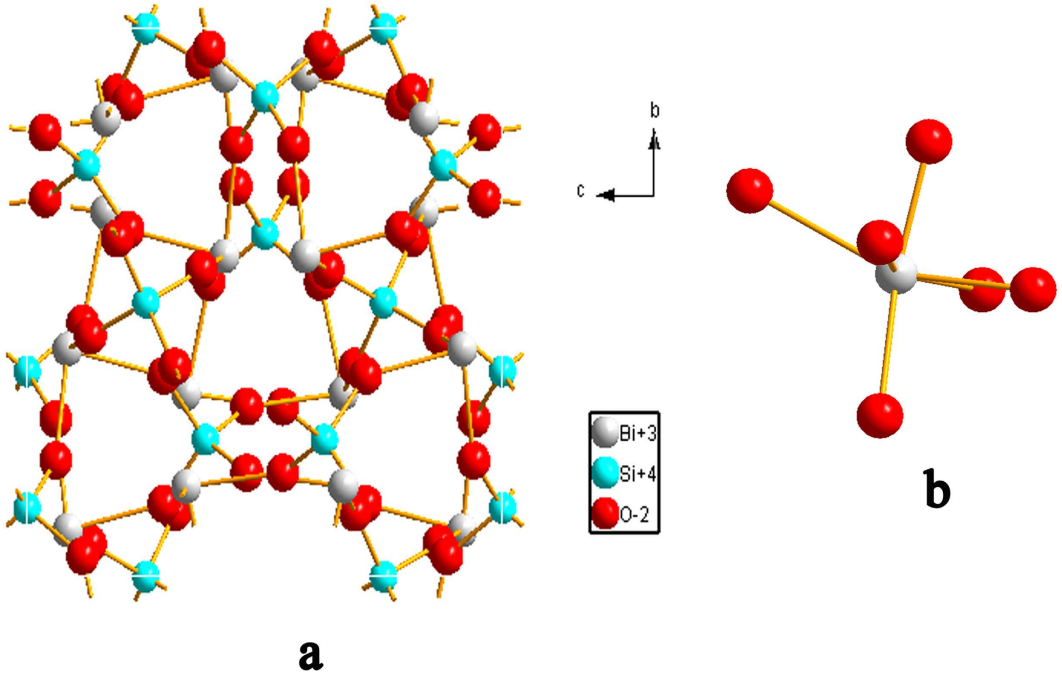

Figure 3. (**a**) Ideal unit cell crystal structure of the $Bi_4Si_3O_{12}$: 2 at% Eu^{3+} phosphor, (**b**) coordination of Bi ions doped with Eu^{3+}.

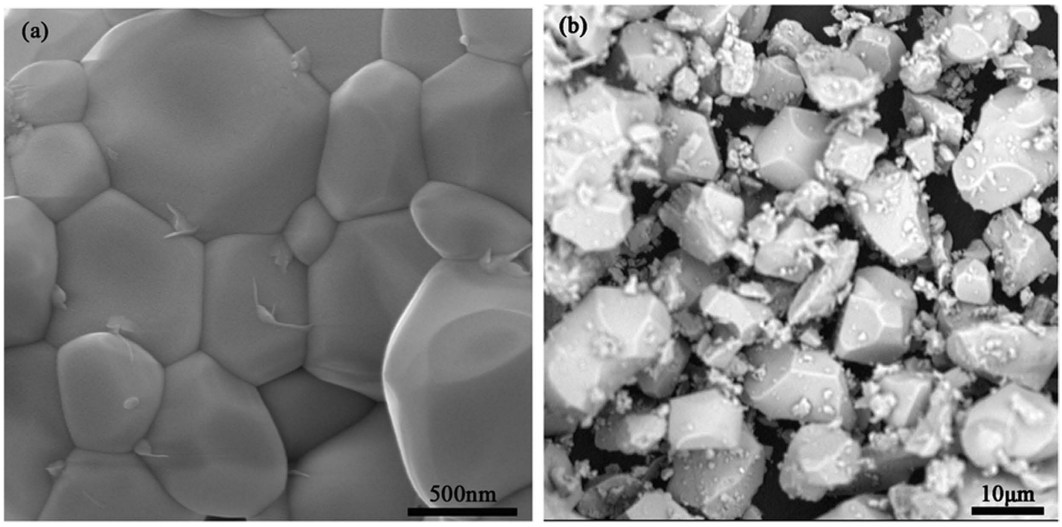

Figure 4. SEM images of $Bi_4Si_3O_{12}$: 2 at% Eu^{3+} phosphors synthesized by (**a**) microwave and (**b**) conventional heating.

rule and spin-orbit coupling, $^1S_0 \rightarrow {}^1P_1$ and $^1S_0 \rightarrow {}^3P_1$ transitions are expected[43]. The $^1S_0 \rightarrow {}^3P_0$ and $^1S_0 \rightarrow {}^3P_2$ transitions remain forbidden if configuration interaction is not taken into account[44]. However, the number and the position of Bi^{3+} absorption bands are sensitive to the coordination polyhedra offered by the host lattice[45]. It was reported that in pure $Bi_4Si_3O_{12}$, the Bi^{3+} absorption band is at 285 nm[32]. An increase in covalency of Bi^{3+}- O band in $Bi_4Si_3O_{12}$: Eu^{3+} shifts this transition to lower energy due to the nephelauxetic effect[46]. Thus, the broad absorption band at 297 nm observed in the $Bi_4Si_3O_{12}$: Eu^{3+} phosphors are assigned to the transition $^1S_0 \rightarrow {}^3P_1$. In comparison with pure BSO samples, the $^1S_0 \rightarrow {}^3P_1$ transition band for $Bi_4Si_3O_{12}$: Eu^{3+} becomes broader and the absorption edge moves from 300 to 350 nm. The similar phenomena can be found in silicates, e.g., $LiYSiO_4$[47], $Na_3YSi_3O_9$[48], where only the $^1S_0 \rightarrow {}^3P_1$ transition are observed. The other broad band with maximum at 271 nm corresponds to charge transfer (CT) transition within the $[O^{2-} \rightarrow Eu^{3+}]$ complex. The excitation spectra of Eu^{3+} exhibit weak and narrow peaks caused by the direct excitation of the Eu^{3+} ground state into various higher levels of the 4*f* manifold. The sharp peaks centered at about 362, 383, 393, 413 nm are ascribed to the intra-configurational 4*f*–4*f* transitions in Eu^{3+} ion, which are $^7F_0 \rightarrow {}^5D_4$, $^7F_0 \rightarrow {}^5L_7$, $^7F_0 \rightarrow {}^5L_6$, and $^7F_0 \rightarrow {}^5D_3$ transitions of Eu^{3+}, respectively. Though

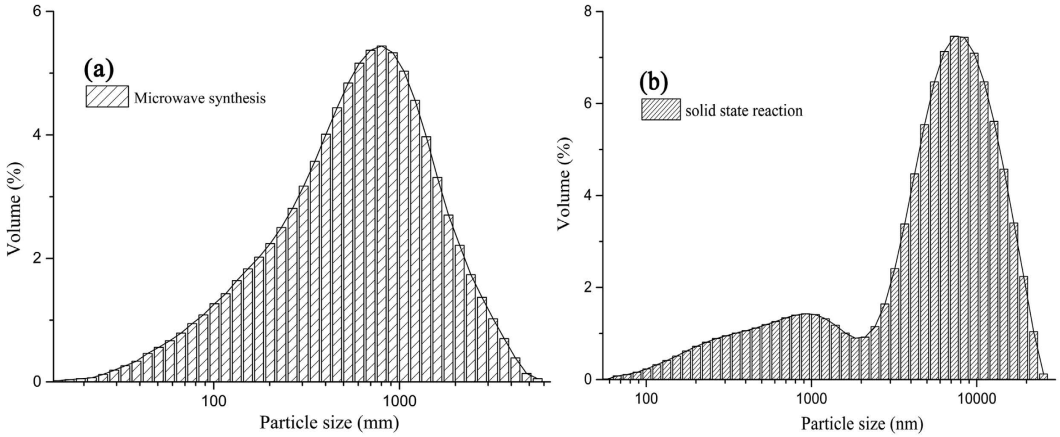

Figure 5. Particle size distribution histograms of $Bi_4Si_3O_{12}$: 2 at% Eu^{3+} phosphor synthesized by (**a**) microwave heating and (**b**) conventional solid-state reaction methods.

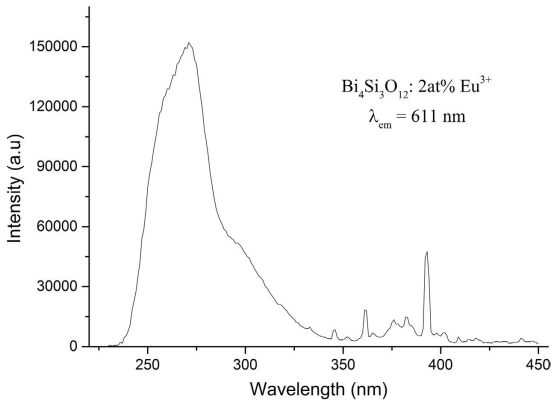

Figure 6. Excitation spectra of $Bi_4Si_3O_{12}$: 2 at% Eu^{3+} phosphors at room temperature.

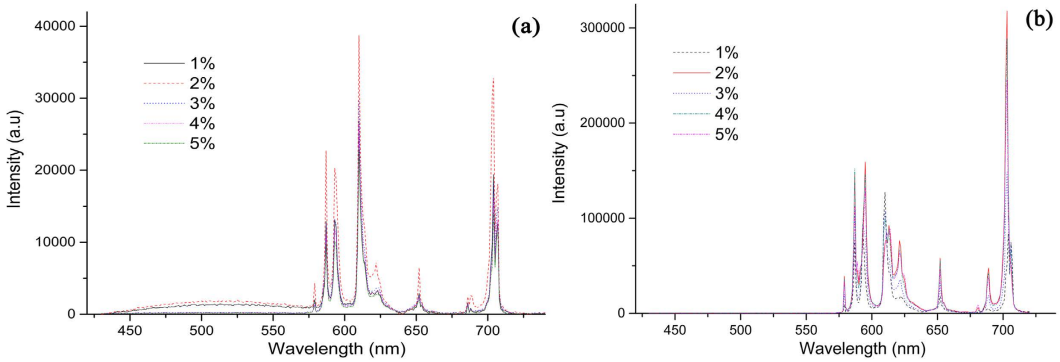

Figure 7. Emission spectra of $Bi_4Si_3O_{12}$: xEu^{3+} ($x = 1$ at%, 2 at%, 3 at%, 4 at%, 5 at%) phosphors under 271 nm (**a**) and 393 nm (**b**) excitation at room temperature

parity-forbidden *f*–*f* transitions of Eu^{3+} ions result in low absorption efficiency in the NUV and blue light, which would lead to potentially severe back scattering losses in LED packages and LED die, it may be improved by extra absorption involving the Bi–O component and CT band to broaden the absorption band. It makes the phosphor absorb NUV light efficiently and matches well with the NUV output wavelength of commercial LED chip.

The emission spectra of the $Bi_4Si_3O_{12}$: xEu^{3+} ($x = 1, 2, 3, 4, 5\%$) under excitation at 271 nm (corresponding to CTB of Eu^{3+} ion) and 393 nm excitation (corresponding to the *f*–*f* transition of Eu^{3+} ion) were presented in Fig. 7 at room temperature. Both emission spectra show characteristic emission of Eu^{3+}. corresponding to the transitions starting from the excited state $^5D_0$ of Eu^{3+} to the lower levels ^7F_J ($J = 0$–4). More interestingly, the Eu^{3+} doped $Bi_4Si_3O_{12}$ shows different luminescence properties upon different excitation wavelengths in these two spectra. The

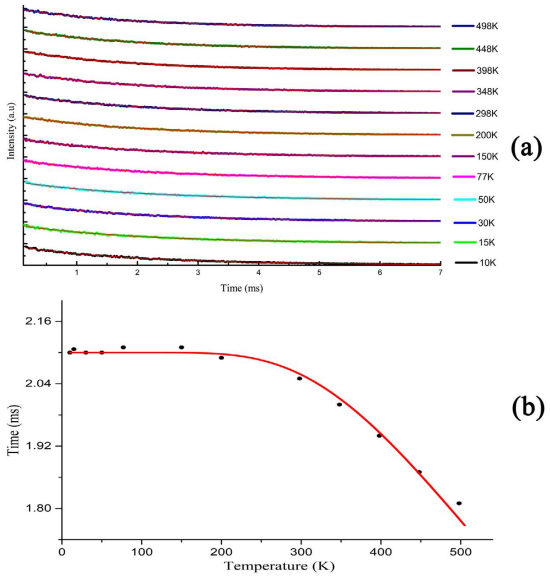

Figure 8. (**a**) Luminescence decay curves of $Bi_4Si_3O_{12}$: 2 at% Eu^{3+} phosphor measured at 10–498 K by excitation at 393 m monitoring the $^5D_0$–$^7F_2$ emission, (**b**) Luminescence decay lifetime as a function of temperature for $Bi_4Si_3O_{12}$: 2 at% Eu^{3+}. The dots are experimental data and the solid curve is the fit to the Eq. 2 in the text.

emission line at 579 nm corresponds to the $^5D_0 \rightarrow {}^7F_0$ transition, and the presence of a single emission line for this transition confirms the Eu^{3+} ions occupy single crystallographic site in the lattice[49]. From Fig. 7(a), it is observed that the Eu^{3+} doped $Bi_4Si_3O_{12}$ presents the dominant strong orange magnetic dipole (MD) transition at 594 nm upon the excitation of CTB at 271 nm. Figure 7(b) shows quite different results, with intense red forced electric dipole (ED) transition upon the excitation of 393 nm. It is interesting to notice that the predominant emission (forced ED transition at 611 nm or MD transition at about 594 nm) depends on not only the site symmetry of the Eu^{3+} ions but also the excitation wavelength. The intensity of $^5D_0 \rightarrow {}^7F_2$ ED transition is strongly influenced by the local structure and the site symmetry around the Eu^{3+} ion while the intensity of $^5D_0 \rightarrow {}^7F_1$ magnetic dipole transition is nearly independent of the host environment. The only one site (16c) for cation is occupied by Bi^{3+} with C_1 site symmetry based on crystallographic structure of $Bi_4Si_3O_{12}$. And no impurity phase in synthesis sample was found according to the XRD analysis. Thus, the difference observed in the emission characteristics of Eu^{3+} in $Bi_4Si_3O_{12}$ under different excitation wavelengths could be explained by the delocalization effect in the excited state that results in the change of original C_1 symmetry of Bi^{3+} site into a new micro-distortion site[50]. The emission spectra excited 271 nm exhibit a broad emission band at about 520 nm, which can be attributed to the typical emission of Bi^{3+} ions in accordance with a previous study[51]. While as the excitation wavelength changes to 393 nm, this emission corresponding to Bi^{3+} ions is gone. Besides peak position, the peak intensity also tightly depend on the excitation wavelength. The relative intensity of the emission peak excited with 393 nm wavelength was almost 8.5 times stronger than the emission peak excited with CTB. It implies that energy transfer from Bi^{3+} to Eu^{3+} ions happened and Bi^{3+} ions plays a dual role of luminescence center and a sensitizer for Eu^{3+} ions.

Luminescence decay analysis. The temperature dependence of the decay profiles of 2 at% Eu^{3+} doped $Bi_4Si_3O_{12}$ phosphor have been measured. The fluorescence decay curves corresponding to $^5D_0 \rightarrow {}^7F_2$ transition around 611 nm upon 393 nm excitation were presented in Fig. 8(a). All decay curves measured can be described to good approximation to a single exponential function in the temperature 10–498 K, which confirms that Eu^{3+} occupy only one site. The lifetime value can be fitted as:

$$I = I_0 + Aexp(-t/\tau) \tag{1}$$

where I_0 is the initial emission intensity for $t = 0$ and τ is the lifetime. The lifetime values are plotted in Fig. 8(b) as a function of recording temperature. As can been seen from Fig. 8(b), the lifetime is nearly temperature independent from 10 to 200 K and then it drops quickly with increasing temperature. The rapid drop of the Eu^{3+} emission lifetime for $T > 200$ K indicates the presence of a typical temperature quenching behavior between Eu^{3+} ions. In the thermal quenching process, energy transfer occurs from Eu^{3+} to killer centers or to any other defect centers near the Eu^{3+} ions by thermal phonon assistance.

Lifetime of the photoluminescence emission from the lowest excited state level can be defined as the inverse of the total radiative and nonradiative transition rates, and the non-radiative relaxation process is in competition with the radiative process. The temperature-dependent luminescence lifetime is fitted to the equation as:

$$\frac{1}{\tau} = \frac{1}{\tau_r} + \frac{1}{\tau_{nr}} exp\left(-\frac{\Delta E}{k_B T}\right) \tag{3}$$

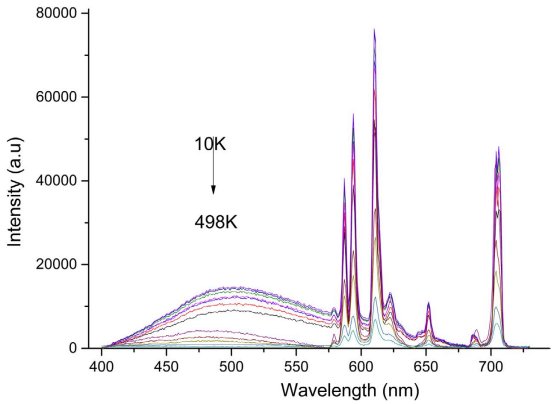

Figure 9. Emission spectra of $Bi_4Si_3O_{12}$: 2 at% Eu^{3+} phosphors at different temperatures.

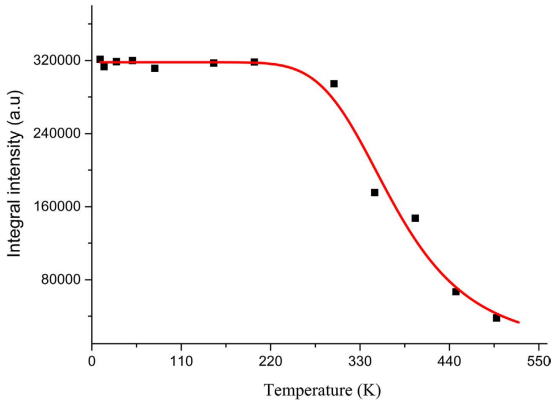

Figure 10. Temperature dependence of the integral emission intensity of 2 at% Eu^{3+}-doped $Bi_4Si_3O_{12}$ phosphors excited by 271 nm (squares) and the result of the fitting according to Eq. (4) (solid line).

where ΔE is the energy gap between the energy levels, k_B is the Boltzmann constant, $1/\tau_r$ and $1/\tau_{nr}$ are the radiative and nonradiative decay rates, respectively. The probability for radiative process is assumed to be constant with temperature for a given material, whereas non-radiative transition is highly dependent on temperature. All relevant parameters are determined by least square fittings using a single exponential function. The fit to the experimental data according to Eq. (2) yields the following results: $\tau_r = 2.14$ ms, $\tau_{nr} = 0.23$ ms, and $\Delta E = 1769\,cm^{-1}$ which is much higher than that of β–Ga_2O_3: Eu^{3+} ($360\,cm^{-1}$)[52]. Similar studied results are obtained from the temperature dependence of the time decay for $Ca_2Ge_7O_{16}$: Eu^{3+} phosphors ($1556\,cm^{-1}$)[53]. According to Laporte selection rule for the electric-dipole (ED) *f*–*f* transitions, long luminescence decay is characteristic of the more symmetrical surrounding while short decay values are observed when site distortion occurs. The local symmetry around Eu^{3+} dopant is not centrosymmetric in β–Ga_2O_3: Eu^{3+}, $Ca_2Ge_7O_{16}$: Eu^{3+} and $Bi_4Si_3O_{12}$: Eu^{3+} phosphors. However, Eu^{3+} occupied distorted octahedral site of Ga^{3+} ion in β–Ga_2O_3, and site distortion results in short lifetime and low activation energy[52]. Eu^{3+} ions substitute for Ca^{2+} ions easily in the lattice of $Ca_2Ge_7O_{16}$ considering their similar radium, and co-doping Li^+ ions can help to incorporate Eu^{3+} ions into Ca^{2+} sites and suppress the non-radiative processes. Thus, the values of lifetime and thermal activation energy of $Bi_4Si_3O_{12}$: Eu^{3+} are close to the reported values in Eu^{3+}-doped $Ca_2Ge_7O_{16}$.

Thermal quenching mechanism. Thermal stability of LED phosphor is one of the most important factors. For example, when high-power white LEDs operate, the temperature of the chip-phosphor package can reach above 423 K[54]. Thus, it is important to evaluate the thermal stability of phosphor for practical application. The emission spectra of 2 at% $Bi_4Si_3O_{12}$: Eu^{3+} phosphors, measured at various temperatures ranging from 10 to 498 K and recorded at the excitation of 271 nm, are presented in Fig. 9. The positions of emission peaks at various temperatures remain almost unchanged, but temperature increase leads to the broadening of emission spectral bands. The broadening in spectral width and the decrease in emission intensity with increasing temperature can be described by thermal quenching[55]. With respect to the relationship between emission intensity for $^5D_0 \rightarrow {}^7F_2$ and surrounding temperature, plotted in Fig. 10, the photoluminescence intensity increased gradually as the temperature declined. The thermal quenching temperature (T_{50}) is defined as the temperature at which the emission intensity is 50% of its original intensity. Thus, the value of the thermal quenching temperature can be deduced from the intensity of emission peaks at different temperature in Fig. 9. The thermal quenching temperature T_{50} was found to be 398 K. When the temperature increases to 498 K, the luminescence intensity of the $Bi_4Si_3O_{12}$: 2 at% Eu^{3+} phosphor is down to about 88% in comparison to that obtained at 298 K.

Thermal quenching effect referred to as temperature-dependent nonradiative processes. The typical nonradiative relaxation mechanisms of Eu^{3+} emission are (i) multiphonon relaxation, (ii) temperature dependent energy transfer, and (iii) crossover from the $4f^6$ electronic configuration of Eu^{3+} ion to a charge transfer state. As can be seen from the Fig. 8(a), the fluorescence decay curves for the $^5D_0$ state in 2 at% Eu^{3+}-doped phosphor at various temperatures can be fitted well with either exactly or very nearly single exponential functions. The possibility that the observed temperature dependence of the nonradiative relaxation might be due to energy transfer to ligands or acceptor traps is doubted, since such a process result in a noticeable deviation from single exponential behavior[56].

The temperature-dependent multiphonon relaxation process could be explained in the following manner[57]:

$$w_{NR} = w_{NR}(0)\left[1 + \left(exp\left(\frac{h\omega_{max}}{k_B T}\right)\right)^{-1}\right]^p \tag{4}$$

where W_{NR} is non-radiative decay rates, $W_{NR}(0)$ is the multiphonon decay rate at 0 K, $h\omega_{max}$ represents the maximum phonon energy of all lattice vibrations in the molecule, k_B is the Boltzmann constant, and T is the temperature, p is the number of the phonons required to bridge the energy gap between the populated state and the adjacent low-lying state. The maximum phonon energy of the $Bi_4Si_3O_{12}$ is about 991 cm^{-1}, which is associated to the vibration mode of [SiO_4] tetrahedral[58]. In view of the large energy gap (>16,000 cm^{-1}) between the crystal field components of the emitting $^5D_0$ level to the ground state $^7F_2$ level, multiphonon relaxation mechanism seems to be not applicable in this case since more than 16 phonons are necessary to bridge the gap and cause effective quenching. Usually, phonons numbers no more than 6 can provide efficient relaxation in the weak coupling limit appropriate to the rare earth elements[59]. Therefore, it can be concluded that the energy transfer and the multiphonon relaxation are not the main reasons of the temperature quenching.

Having eliminated all other reasonable mechanistic pathways, we assert that the most probable thermal quenching mechanism involved nonradiation relaxation is most likely due to crossover process. The crossover quenching from the $^5D_0$ excited state to a Franck-Condon shifted state is a thermal activation process. In crossover quenching mechanism, the temperature-dependent of the luminescent intensity can be described by the Struck-Fonger model equation[57]:

$$I(T) = \frac{I_0}{1 + Aexp(-\Delta E/k_B T)} \tag{5}$$

where $I(T)$ is the luminescence intensity at a given temperature T, I_0 is the initial luminescence intensity at the temperature of 0 K, A is a constant, k_B is Boltzmann constant, and ΔE is the activation energy for the thermal quenching process, which can be obtained by fitting the thermal quenching data. The experimental data for *f–f* integrated intensity, as shown in Fig. 10, are nonlinearly fitted by Eq. (5). The solid line in Fig. 10 shows the fitting curve. It can be found that the fitting curve matches well with the experimental data. The activation energy ΔE is obtained to be 0.24 eV for $Bi_4Si_3O_{12}$: 2 at %Eu^{3+} phosphor according to a least-square fitting of the formula to the experimental data. The value of the activation energy ΔE is similar to those determined for other silicate based red phosphors, for example, $NaCaGaSi_2O_7$: Eu^{3+}, Li^+ (0.23 eV)[59], $Sr_2Y_8(SiO_4)_6O_2$: Bi^{3+}/Eu^{3+} (0.23 eV)[60], and $CaAl_2Si_2O_8$: Eu^{3+} (0.27 eV)[61]. It illustrates good thermal stability of the obtained $Bi_4Si_3O_{12}$: Eu^{3+} phosphor.

CIE chromaticity coordinate and quantum efficiency of $Bi_4Si_3O_{12}$: 2 at %Eu^{3+} phosphor. As is well known, photoluminescence spectrum for luminescent materials have characteristic temperature dependence, that is, with increasing of the temperature, the position of emission peak move to the lower energy region, the full width at half-maximum (FWHM) of emission band is broadened and the emission intensity is quenched at a certain temperature. These phenomena, thermal broadening, redshift of emission peak and the decrease in emission intensity, can be described by the interaction between the luminescence center and the vibrating crystalline environment[62]. As shown in Fig. 9, with the increase in the temperature from 10 up to 498 K, the emission intensities of $Bi_4Si_3O_{12}$: 2 at% Eu^{3+} decrease, and the FWHM of $Bi_4Si_3O_{12}$: 2 at% Eu^{3+} emission increases. However, positions of emission peak remain approximately constant with increasing temperature. The phonon interaction with the emitting center of Eu^{3+} ion is the dominating factor responsible for intensity quenching and the temperature broadening of $Bi_4Si_3O_{12}$: Eu^{3+} luminescence spectral bands.

To evaluate the influence of temperature on the chromaticity, the CIE chromaticity coordinates of Eu^{3+} doped $Bi_4Si_3O_{12}$ phosphors are calculated according to the emission spectra for temperatures ranging from 298 to 498 K. The movement of the chromaticity point with temperature is shown in Fig. 11. Under excitation of 393 nm, the luminescent color tends to red light due to the increase of the relative intensity of the red component in currently synthesized phosphors. For comparison, the CIE color coordinates of the phosphor under the excitation of CTB are also provided. The CIE color coordinates of $Bi_4Si_3O_{12}$: 2 at% Eu^{3+} vary from orange-red to red with the increase of temperature. Detailed CIE coordinate values upon 271 and 393 nm excitation are listed in Fig. 11. In addition, as evidenced by the excitation spectrum, the currently studied phosphor can effectively absorb the emissions from LED based NUV radiation. As the temperature increases, the interaction between luminescent centers and phonons holds dominant and, consequently the FWHM of the emission peak is broadened[63]. The spectra broadening leads to slight shift of the color point in the chromaticity diagram.

The quantum efficiency values of $Bi_4Si_3O_{12}$: Eu^{3+} phosphor for Eu^{3+} red emission are determined to be 14.5% and 1.6% under excitation at 394 nm and 271 nm, respectively. This fact indicates that the energy absorbed by the CTB is transferred to Eu^{3+} ions levels nonradiatively and the non-radiative losses compared to radiative emission is relatively high in this phosphor under CT excitation. The quantum efficiency of $Bi_4Si_3O_{12}$: Eu^{3+} phosphor under excitation at 394 nm is 14.5%, which is higher than that of commercial red phosphor Y_2O_3: Eu^{3+} (9.6%, 394 nm

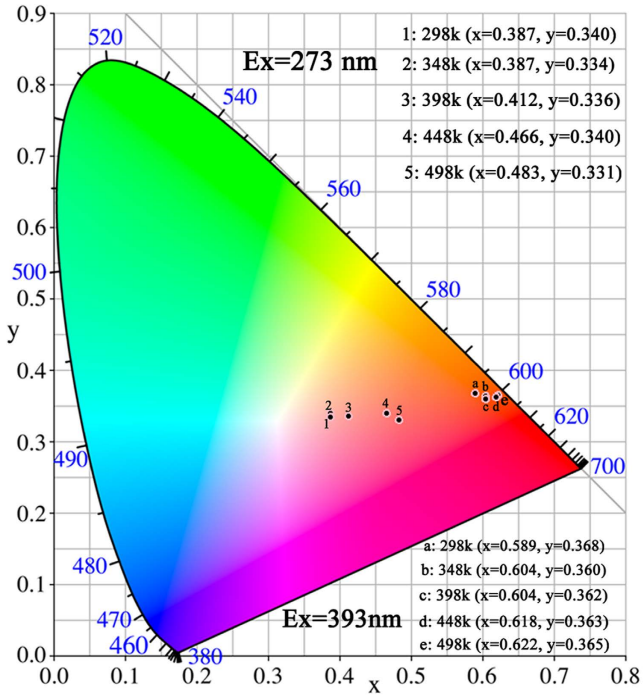

Figure 11. CIE chromaticity diagram of $Bi_4Si_3O_{12}$: 2 at%Eu^{3+} excited by 271 nm and 393 nm at different temperatures.

excitation)[64], Y_2O_2S: Eu^{3+} (4.2%, 395 nm excitation)[65]. However, the quantum efficiency of $Bi_4Si_3O_{12}$: Eu^{3+} is lower than that of the red-emitting nitride phosphor $Sr_2Si_5N_8$: Eu^{2+} (75–80%, 465 nm excitation)[66]. Quantum efficiency of phosphor is often adopted as an important parameter in evaluating its potential application for solid state lighting. The quantum efficiency of $Bi_4Si_3O_{12}$: Eu^{3+} phosphor can be further improved by optimizing synthetic procedure to reduce the surface defect, to get higher crystallization and to control gain morphology and size of phosphor.

Methods

Commercially available high purity reagents (99.99%) of Bi_2O_3, SiO_2 and Eu_2O_3 were used as raw materials to prepare $Bi_4Si_3O_{12}$: xEu^{3+} phosphors (x = 1 at%, 2 at%, 3 at%, 4 at%,5 at%). The powders were weighed according to the chemical formula and ground and mixed together in a ball mill with an agate ball using an agate container for 8 h. After grinding and extruding to form pieces, the mixture was transferred to a small Al_2O_3 crucible that was in turn put into a larger covered Al_2O_3 crucible. The gap between two crucibles was filled with silicon carbide powder as the microwave susceptor. Considering the fact that the microwave penetration depth into silicon carbide layer decreases as the temperature rises, the amount of silicon carbide powder would be selected to ensure that the mixture was adequately received microwave irradiation at a certain temperatures. In order to minimize heat loss, the large crucible was placed in a cavity surrounded by the alumina insulation foam. The temperature was measured by inserting an infrared pyrometer into a small hole at the center of the inner crucible. Finally, the whole setup was placed into in a microwave heater (Synotherm Corp., HAMiLab-V3, China) with a rotating plate and a continuously adjustable output power from 0.2 to 2.8 kW at 650–800 °C for 10–30 minutes in air atmosphere.

The prepared samples were characterized by a Dmax 2500 X-ray diffractometer with CuKα radiation (Rigaku, Japan), with a scanning rate of 5°/min for phase identification and a step-scanning mode of 8 s per step (step size: 0.02°) for Rietveld analysis in the 2θ range from 12° to 90°. The structure refinement was performed using the Rietveld method with the General Structure Analysis System (GSAS) program and its graphical user interface, EXPGUI[67,68]. The grain size of the sample was analyzed by a Mastersizer 2000 laser scattering particle size analyzer (Malvern, UK). The morphology of the Eu^{3+} -doped $Bi_4Si_3O_{12}$ phosphor was characterized using scanning electronic microscope (SEM FEI Quanta 200 FEG, USA). The photoluminescence excitation and emission spectra were recorded using Edinburgh Instruments FLS920 spectrophotometer and a 450 W Xenon lamp was used as an excitation source (EI, UK). Sample cooling was provided by a closed cycle liquid helium optical cryostat which allowed the temperature to be varied between 10 and 650 K (ARS, USA). The fluorescence quantum efficiency measurement by an absolute method was performed using the EI spectrophotometer equipped with an integrating sphere. The sphere with 120 mm diameter spherical cavity was coated with BENFLEC. The quantum efficiency were corrected by a series of direct and indirect measurements to remove the re-excitation of the sample from excitation light reflected within the sphere.

Conclusion

$Bi_4Si_3O_{12}$: Eu^{3+} phosphors have been successfully synthesized by a novel, fast and energy-efficient microwave irradiation method. The roughly spherical $Bi_4Si_3O_{12}$: Eu^{3+} particles with few aggregation or agglomeration have been obtained by this route. The phase analysis and crystal structure of the phosphors were examined by XRD patterns and Rietveld refinement. The prepared samples exhibited single-phase with a cubic structure. The excitation spectrum consists of a broad band ranged from 220 nm to 350 nm, which assigned to the Eu^{3+} charge transfer transition and $6s^2 \rightarrow 6s6p$ transition of Bi^{3+}. and a series of sharp lines corresponding to the intra-configurational $4f$–$4f$ transitions of Eu^{3+}. Characteristic for the Eu^{3+} electric-dipole emission with the maximum at 610 nm was recorded. The luminescence decay of $Bi_4Si_3O_{12}$: Eu^{3+} gradually decreases with increasing temperature, due to the energy transfer among Eu^{3+} ions occurring in a non-radiative process. With increasing of temperature the emission peaks show increasing bandwidth and decreasing intensity, which is due to the electron-phonon interaction with the luminescence center. The $Bi_4Si_3O_{12}$: Eu^{3+} phosphor shows a typical thermal quenching effect with a T_{50} value of 398 K, and the thermal activation energy for the crossover process is calculated to be 0.24 eV. We have found that for the thermal quenching of Eu^{3+} luminescence the crossover relaxation mechanism is mainly responsible. In view of its strong and broad absorption band in the NUV region, intense red light with the appropriate chromaticity coordinate, this phosphor is competitive as a promising candidate for NUV LEDs.

References

1. Schubert, E. F. & Kim, J. K. Solid-state light sources getting smart. *Science* **308,** 1274–1278 (2005).
2. Raju, G. S. R. *et al.* Excitation induced efficient luminescent properties of nanocrystalline Tb^{3+}/Sm^{3+}: $Ca_2Gd_8Si_6O_{26}$ phosphors. *J. Mater. Chem.* **21,** 6136–6139 (2011).
3. Nakamura, S. & Fasol, G. *The Blue Laser Diode: GaN Based Light Emitters and Lasers*. Springer-Verlag: Berlin-Heidelberg, 1997).
4. Nishida, T., Ban, T. & Kobayashi, N. High-color-rendering light sources consisting of a 350-nm ultraviolet light-emitting diode and three-basal-color phosphors. *Appl. Phys. Lett.* **82,** 3817–3819 (2003).
5. Sailaja, S., Dhoble, S. J., Brahme, N. & Reddy, B. S. Synthesis, photoluminescence and mechanoluminescence properties of Eu^{3+} ions activated $Ca_2Gd_2W_3O_{14}$ phosphors. *J. Mater Sci.* **46,** 7793–7798 (2011).
6. Zhang, Q. H., Wang, J., Zhang, M. & Su, Q. Tunable bluish green to yellowish green $Ca_{2(1-x)}Sr_{2x}Al_2SiO_7$: Eu^{2+} phosphors for potential LED application. *Appl. Phys. B* **92,** 195–198 (2008).
7. Wang, Z. L., Liang, H. B., Gong, M. L. & Su, Q. A potential red-emitting phosphor for LED solid-state lighting, Electrochem. *Solid-State Lett.* **8,** H33–H35 (2005).
8. Pust, P. *et al.* Narrow-band red-emitting $Sr[LiAl_3N_4]$: Eu^{2+} as a next-generation LED-phosphor material. *Nature Materials* **13,** 891–896 (2014).
9. Xie, R. J., Li, Y. Q., Hirosake, N. & Yamamoto, H. *Nitride phosphors and solid-state lighting* (Boca Raton: CRC Press, Taylor & Francis Group, LLC; 2011).
10. Nguyen, H. D., Lin, C. C. & Liu, R. S. Waterproof Alkyl Phosphate Coated Fluoride Phosphors for Optoelectronic Materials. *Angew. Chem., Int. Ed.* **54,** 10862–6 (2015).
11. Jiang, X. *et al.* Hydrothermal synthesis and photoluminescence properties of red phosphor $BaSiF_6$: Mn^{4+} for LED applications. *J. Mater. Chem. C* **2,** 2301–2306 (2014).
12. Wang, B. *et al.* Non-Rare-Earth $BaMgAl_{10-2x}O_{17}$: xMn^{4+}, xMg^{2+}: A Narrow-Band Red Phosphor for Use as a High-Power Warm w-LED. *Chem. Mater.* **28,** 3515–3524 (2016).
13. Chen, D. Q. *et al.* Enhanced luminescence of Mn^{4+}: $Y_3Al_5O_{12}$ red phosphor via impurity doping. *J. Mater. Chem. C* **4,** 1704–1712 (2016).
14. Li, Y. Q. *et al.* Luminescence properties of red-emitting $M^2Si^5N^8$: Eu^{2+} (M = Ca Sr, Ba) LED conversion phosphors. *J Alloys Compd.* **417,** 273–27 (2006)
15. Piao, X. *et al.* Preparation of $CaAlSiN_3$: Eu^{2+} Phosphors by the Self-Propagating High-Temperature Synthesis and Their Luminescent Properties. *Chem. Mater.* **19,** 4592–4599 (2007).
16. Kim, Y. S. *et al.* Red-emitting (Sr, Ca)$AlSiN_3$: Eu^{2+} phosphors synthesized by spark plasma sintering. *ECS J Solid State Sci. Technol* **2,** R3021–R3025 (2013).
17. Liu, R. S., Liu, Y. H., Bagkar, N. C. & Hu, S. F. Enhanced luminescence of $SrSi_2O_2N_2$: Eu^{2+} phosphors by codoping with Ce^{3+}, Mn^{2+}, and Dy^{3+} ions. *Appl. Phys. Lett.* **91,** 061119-1-3 (2007)
18. Chen, D. Q., Zhou, Y. & Zhong, J. S. A review on Mn^{4+} activators in solids for warm white light-emitting diodes. *RSC Adv.* **6,** 86285–86296 (2016).
19. Zukauskas, A., Vaicekauskas, R., Ivanauskas, F., Vaitkevicius, H. & Shur, M. S. Spectral optimization of phosphor-conversion light-emitting diodes for ultimate color rendering. *Appl. Phys. Lett.* **93,** 051115-1-3 (2008).
20. Seo, H. J. Line broadening and crystallographic sites for Eu^{3+} in disordered double borate $Ca_3Gd_2(BO_3)_4$. *J. Alloys Compd.* **604,** 100–105 (2014).
21. Xu, X. T., Tang, Y. X. & Mo, F. W. Synthesis and luminescent properties of $CaTiO_3$: Eu^{3+}, Al^{3+} phosphors. *Ceram. Int.* **40,** 10887–10892 (2014).
22. Geng, J., Yu, C. S., Wu, H., Wu, B. J. & Tian, L. H. Photoluminescence characteristics of red-emitting Eu^{3+}-activated $Ca_4GdNbMo_4O_{20}$ phosphor. *J. Lumin.* **140,** 71–73 (2013).
23. Krasnikov, A., Shalapska, T., Stryganyuk, G., Voloshinovskii, A. & Zazubovich, S. Photoluminescence and energy transfer in Eu^{3+}-doped alkali gadolinium phosphates. *Phys. Status Solidi B* **250,** 1418–1425 (2013).
24. Zhang, Y. *et al.* Structure and photoluminescence properties of $KSr_4(BO_3)_3$: Eu^{3+} red-emitting phosphor. *Opt. Mater. Express* **2,** 92–102 (2012).
25. Huang, Y., Nakai, Y., Tsuboi, T. J. & Seo, H. J. The new red-emitting phosphor of oxyfluoride $Ca_2RF_4PO_4$: Eu^{3+} (R = Gd, Y) for solid state lighting applications. *Opt. Express* **19,** 6303–11 (2011).
26. Chen, H. Y., Weng, M. H., Chang, S. J. & Yang, R. Y. Preparation of Sr_2SiO_4: Eu^{3+} phosphors by microwave-assisted sintering and their luminescent properties. *Ceram. Int.* **38,** 125–130 (2012).
27. Feng, G., Jiang, W. H., Chen, Y. B. & Zeng, R. J. A novel red phosphor $NaLa_4(SiO_4)_3F$: Eu^{3+}. *Mater. Lett.* **65,** 110–112 (2011).
28. Senguttuvan, N. *et al.* Crystal growth and optical properties of $Bi_4Si_3O_{12}$: Nd. *J. Cryst. Growth* **229,** 188–192 (2001).
29. Ishii, M., Harada, K., Senguttuvan, N., Kobayashi, M. & Yamaga, I. Crystal growth of BSO ($Bi_4Si_3O_{12}$) by vertical Bridgman method. *J. Cryst. Growth* **205,** 191–195 (1999).
30. Zhang, Y., Xu, J. Y. & Shao, P. F. Growth and spectroscopic properties of Yb: BSO single crystal. *J. Cryst. Growth* **318,** 920–923 (2011).
31. Zhang, Y., Xu, J. Y. & Lu, B. L. Spectroscopic properties of Dy^{3+}: $Bi_4Si_3O_{12}$ single crystal. *J. Alloys Compd.* **582,** 635–639 (2014).
32. Kobayashi, M., Ishii, M., Harada, K. & Yamaga, I. Bismuth silicate $Bi_4Si_3O_{12}$, a faster scintillator than bismuth germanate $Bi_4Ge_3O_{12}$. *Nucl. Instrum. Meth. A* **372,** 45–50 (1996).
33. Xie, H. D., Jia, C. X., Jiang, Y. R. & Wang, X. C. Synthesis of $Bi_4Si_3O_{12}$ powders by a sol-gel method. *Mater. Chem. Phys.* **133,** 1003–1005 (2012).

34. Leadbeater, N. E. *Microwave Heating as a Tool for Sustainable Chemistry*, (CRC: Boca Raton, 2010).
35. Snyder, W. B. Jr., Sutton, W. H., Iskander, M. F. & Johnson, D. L. Microwave Processing of Materials II. *Materials Research Society Proceedings*, MRS: Pittsburgh (1990).
36. Wu, H. Q., Cao, P. P., Zhang, N., Mao, L. & Li, M. M. Controlled synthesis and magnetic properties of $Co_{1-x}Ni_x$/MWCNT nanocomposites by microwave irradiation. *Mater. Res. Bull.* **47,** 1–5 (2012).
37. Xu, L., Xu, H. Y. & Wang, H. A Simple and Rapid Synthetic Route to Nanocrystalline TiO_2 by Microwave Irradiation. *Adv. Mater. Res.* **583,** 354–357 (2012).
38. Sadhu, A. *et al.* Ferromagnetism in Lightly Doped $Pr_{1-x}Ca_xMnO_3$ (x = 0.023, 0.036) Nanoparticles Synthesized by Microwave Irradiation. *Chem. Mater.* **24,** 3758–3764 (2012).
39. Ananth, K. P., Jose, S. P., Venkatesh, K. S. & Ilangovan, R. Size Controlled Synthesis of Magnetite Nanoparticles Using Microwave Irradiation Method. *J. Nano Res.* **24,** 184–193 (2013).
40. Suryawanshi, Y. R. *et al.* Microwave irradiation solvothermal technique: an optimized protocol for size-control synthesis of Ru nanoparticles. *Cryst. Res. Technol.* **48,** 69–74 (2013).
41. Prakash, T., Jayaprakash, R., Espro, C., Neri, G. & Kumar, E. R. Effect of Sn doping on microstructural and optical properties of ZnO nanoparticles synthesized by microwave irradiation method. *J. Mater. Sci.* **49,** 1776–1784 (2014).
42. Meltzer, R. S., Feofilov, S. P., Tissue, B. & Yuan, H. D. Dependence of fluorescence lifetimes of Y_2O_3: Eu^{3+} nanoparticles on the surrounding medium. *Phys. Rev. B*, **60,** R14012–R14015 (1999).
43. Seitz, F. Interpretation of the Properties of Alkali Halide-Thallium Phosphors. *J. Chem. Phys.* **6,** 150–162 (1938).
44. Blasse, G. & Grabmaier, B. C. *Luminescent Materials*. Springer-Verlag: Berlin-Heidelberg, 1994).
45. Jorgensen, C. K. *Absorption Spectra and Chemical Bonding in Complexes*. Pergamon: New York, 1962).
46. Frey, S. T. & Horrocks, W. D. On correlating the frequency of the $^7F_0 \rightarrow {}^5D_0$ transition in Eu^{3+} complexes with the sum of "nephelauxetic parameters" for all of the coordinating atoms. *Inorg. Chim. Acta.* **229,** 383–390 (1995).
47. Blasse, G. The Ultraviolet Absorption Bands of Bi^{3+} and Eu^{3+} in Oxides. *J. Solid State Chem.* **4,** 52–54 (1972).
48. Kim, C. H., Park, H. L. & Mho, S. Photoluminescence of Eu^{3+} and Bi^{3+} in $Na_3YSi_3O_9$. *Solid State Commun.* **101,** 109–113 (1997).
49. Blasse, G. Influence of local charge compensation on site occupation and luminescence of apatites. *J. Solid State Chem.* **14,** 181–184 (1975).
50. Lin, H., Liang, H., Zhang, G. & Su, Q. The luminescence of Eu^{3+} activated $Ba_2Mg(BO_3)_2$ phosphors. *Appl. Phys. A* **105,** 143–147 (2011).
51. Blasse, G. & Bril, A. Investigations on Bi^{3+}-activated phosphors. *J. Chem. Phys.* **48,** 217–222 (1968).
52. Zhu, H. M., Li, R. F., Luo, W. Q. & Chen, X. Y. Eu^{3+}-doped β-Ga_2O_3 nanophosphors: annealing effect, electronic structure and optical spectroscopy. *Phys. Chem. Chem. Phys.* **13,** 4411–4419 (2011).
53. Wang, T., Xu, X. H., Zhou, D. C., Qiu, J. B. & Yu, X. Red phosphor $Ca_2Ge_7O_{16}$: Eu^{3+} for potential application in field emission displays and white light-emitting diodes. *Mater. Res. Bull.* **60,** 876–881 (2014).
54. Rohwer, L. S. & Srivastava, A. M. Development of phosphors for LEDs. *The Electrochemical Society Interface*. summer, 37–40 (2003)
55. Shionoya, S. & Yen, W. M. *Phosphor Handbook*. CRC: Boca Raton, 1998).
56. Berry, M. T., May, P. S. & Xu, H. Temperature Dependence of the Eu^{3+} 5D0 Lifetime in Europium Tris (2, 2, 6, 6-tetramethyl-3, 5-heptanedionato). *J. Phys. Chem.* **100,** 9216–9222 (1996).
57. Fonger, W. H. & Struck, C. W. Eu^{3+} 5D Resonance Quenching to the Charge-Transfer States in Y_2O_2S, La_2O_2S, and LaOCl. *J. Chem. Phys.* **52,** 6364–6372 (1970).
58. Beneventi, P., Bersani, D., Lottici, P. P. & Kovacs, L. A Raman Study of $Bi_4(Ge_x, Si_{1-x})_3O_{12}$ Crystals. *Solid State Commun.* **93,** 143–146 (1995).
59. Yeh, K. Y. & Liu, W. R. Luminescence properties of $NaCaGaSi_2O_7$: RE, Li^+ (RE = Ce^{3+}, Eu^{3+} or Tb^{3+}) phosphors for UV excitable white light emitting diodes. *Mater. Res. Bull.* **80,** 127–134 (2016).
60. Li, K., Fan, J., Shang, M. M., Lian, H. Z. & Lin, J. $Sr_2Y_8(SiO_4)_6O_2$: Bi^{3+}/Eu^{3+}: a single-component white-emitting phosphor via energy transfer for UV w-LEDs. *J. Mater. Chem. C* **3,** 9989–9998 (2015).
61. Dai, W. B., Zhou, M., Xian, Z. Y. & Zeng, L. K. Structure and photoluminescence characteristics of europium(III) doped in $CaAl_2Si_2O_8$ phosphors. *RSC Adv.*, **4,** 25470–25478 (2014).
62. Mikhailik, m, V. B. *et al.* One- and two-photon excited luminescence and band-gap assignment in $CaWO_4$. *Phys. Rev. B* **69,** 205110–9 (2004).
63. Kim, J. S. *et al.* Luminescent and thermal properties of full-color emitting $X_3MgSi_2O_8$: Eu^{2+}, Mn^{2+} (X = Ba, Sr, Ca) phosphors for white LED. *J. Lumin.* **122–123,** 583–586 (2007).
64. Long, S., Hou, J., Zhang, G., Huang, F. & Zeng, Y. High quantum efficiency red-emission tungstate based phosphor $Sr(La_{1-x}Eu_x)_2Mg_2W_2O_{12}$ for WLEDs application. *Ceram. Int.* **39,** 6013–6017 (2013).
65. Zhang, L. *et al.* Structure evolution and tunable luminescence of $(Sr_{0.98-m}Ba_mEu_{0.02})_2Ca(Mo_{1-n}W_n)O_6$ phosphor with ultraviolet excitation for white LEDs. *J. Alloys Compd.* **558,** 229–235 (2013).
66. Li, Y. Q. *et al.* Luminescence properties of red-emitting $M_2Si_5N_8$: Eu^{2+} (M = Ca, Sr, Ba) LED conversion phosphors. *J. Alloys Compd.* **417,** 273–279 (2006).
67. Larson, A. C. & Von Dreele, R. B. *General Structure Analysis System (GSAS) (Report LAUR 86-748)*; Los Alamos National Laboratory: Los Alamos, NM, 2001.
68. Toby, B. H. & EXPGUI, A. Graphical User Interface for GSAS. *J. Appl. Crystallogr.* **34,** 210–213 (2001).

Acknowledgements

The authors would like to acknowledge Dr. Bo Wei (CHANGSHU INSTITUTE OF TECHNOLOGY) for X-ray powder diffraction (XRD) measurements. This work was supported by the Shanghai Municipal Education Commission (14YZ145), Natural Science Foundation of Shanghai (16ZR1435900) and National Natural Science Foundation of China (51572175).

Author Contributions

Y.Z. coordinated and designed the experiments. Y.Z. and Q.Z.C. synthesized the phosphors. Y.Z. and B. B.Y. performed the measurements. J. Y. X. provide advice and consultation. Y.Z. wrote the main manuscript text. All authors discussed the result and commented on the manuscript.

Additional Information

Competing financial interests: The authors declare no competing financial interests.

How to cite this article: Zhang, Y. *et al.* Eu^{3+}-doped $Bi_4Si_3O_{12}$ red phosphor for solid state lighting: microwave synthesis, characterization, photoluminescence properties and thermal quenching mechanisms. *Sci. Rep.* **7**, 42464; doi: 10.1038/srep42464 (2017).